*Research Article*

# Interdecadal Variation of Spring Extreme High-Temperature Events in the Western Tianshan Mountains and Its Relationship with the Tropical SST

**Liyun Ma** [iD] **,**[1] **Ping Chen,**[1] **Junqiang Yao,**[1] **Jinggao Hu,**[2] **and Weiyi Mao** [iD] [1]

[1]*Institute of Desert Meteorology, China Meteorological Administration, Ürümqi 830002, China*
[2]*Key Laboratory of Meteorological Disaster, Ministry of Education (KLME)/Joint International Research Laboratory of Climate and Environment Change (ILCEC)/Collaborative Innovation Center on Forecast and Evaluation of Meteorological Disasters (CIC-FEMD), Nanjing University of Information Science & Technology, Nanjing 210044, China*

Correspondence should be addressed to Weiyi Mao; mao6991@vip.sina.com

This study performed an observational analysis to examine the interdecadal variation in the frequency of extreme high-temperature events (EHEs) during spring over the western Tianshan mountain, China, which were characterized by relatively fewer (more) EHEs during 1983–1996 (2000–2015). A composite analysis indicated that the interdecadal increase in EHEs is closely related to a deep dynamic anomalous Iranian high. Under the control of this high system, the water vapor content decreased over the western Tianshan mountains, and atmospheric circulation was dominated by a descending motion. Both were attributed to the decreased cloud cover, inducing a cloud-forced net solar radiation increase. The short-wave radiation flux and sensible heat flux reaching the surface increased, and the net surface heat flux increased cumulatively, which was conducive to the surface temperature increase and EHE occurrence. The anomalous Iranian high responsible for ECEs occurrence was related to the air-sea interaction over the Atlantic and Indo-Pacific. The latitudinal sea surface temperature (SST) difference between the tropical western Pacific and the western Indian Ocean directly strengthens the Walker circulation and thus enhances the Iranian high. In addition, the anomalous Iranian high was affected by the atmospheric wave trains at middle latitude, which was triggered by the warm anomaly of the Atlantic SST.

## 1. Introduction

The Intergovernmental Panel on Climate Change's Sixth Assessment Report points out that extreme events, such as heatwaves, droughts, heavy precipitation, and tropical cyclones, have increased [1]. In recent decades, extreme high temperatures have had a major impact on human health, agriculture, ecological environment, and socioeconomic zones [2, 3]. For example, European heatwaves in 2003 and 2010 killed tens of thousands of people [4, 5], and in 2021, the super heatwave event in western North America killed hundreds of people and caused forest fires [6]. On the one hand, spring's extreme high temperature affects the growth time of spring wheat and reduces the yield, negatively affecting agricultural production [7]. On the other hand, high temperature may intensify snow and ice melting in the source regions of rivers, causing flood disasters such as snowmelt (ice) floods and ice dam breaks [8, 9].

As changes in extreme climate/weather events have greater impacts on human life than the variation of the climate mean state, it is of great significance to investigate the variations of extreme events. According to previous research studies, high temperatures have been reported to rise on an interdecadal basis in eastern China [2, 10], northeastern China [11], southern China [12], and northwestern China [13], but the increasing rates are different. In northern and southwestern China, the frequency of extreme high-temperature events (EHEs) is increasing quickly, while

it increases slowly in southern China [11]. The Xinjiang Uygur autonomous region, located in northwest China, also shows a noticeable increase in high-temperature events [14]. The variation trend of the EHEs can change the pattern of snowmelt floods in Xinjiang [8, 15]. Therefore, it is of great social significance to focus on the spatiotemporal variations of spring extreme high temperatures in Xinjiang and understand their internal mechanisms.

The occurrence of EHEs is closely related to atmospheric circulations, and atmospheric circulation anomalies are a direct cause of weather and climate changes [16]. However, the circulation characteristics that cause the EHEs are different in different regions of China [17]. In Northeast China, positive geopotential height anomaly/anticyclonic circulation anomaly in the middle and upper troposphere is closely associated with the EHEs. Anticyclonic circulation anomalies affect atmospheric descending motion and reduce cloud cover, leading to adiabatic heating, increasing solar radiation, and thus increasing surface temperature [16]. From central to southern China, the lower troposphere's temperature advection has an impact on the EHEs as well [18]. In eastern and southern China, the EHEs are affected by the western Pacific subtropical high (WPSH) anomaly [19, 20]. The atmospheric circulation anomalies that contribute to the EHEs in China are related to several elements, including the tropical Pacific sea surface temperature (SST) [18, 21], El Niño-southern oscillation [22, 23], Pacific El Niño-like pattern [24], Atlantic SST [25], tropical Indian Ocean SST [26], and sea ice [27, 28]. SST anomalies in the tropical Indian Ocean enhance latent heat to excite the Rossby wave train, resulting in the anomalies of the South Asian high and WPSH, and thus affecting the summer EHEs in eastern China [23]. The East Asia-Pacific/Pacific-Japan teleconnection may cause anticyclonic anomalies and atmospheric sinking in southern China as a result of the maritime continent's abnormal warming, favoring EHEs there [12].

Previous studies on the EHEs in Xinjiang, Northwest China, mostly focused on the spatial distribution characteristics and temporal variation trends of the EHEs [8, 29–31], but less research has been conducted on the atmospheric circulation anomalies of the EHEs and the related mechanisms. A few studies indicate that the anomalous variations of the Iran high and South Asia high are of guiding significance for the evolution of high temperature processes in Xinjiang [32, 33].

The western Tianshan Mountains in Xinjiang, China, namely, the confluence of the Yili River in central Xinjiang and the Tarim River in southern Xinjiang, are an essential agricultural and animal husbandry production area in Xinjiang [34, 35]. Therefore, paying attention to the spring EHEs in the western Tianshan area is of great significance for flood prevention and mitigation, as well as for agricultural production and life. In recent decades, the interdecadal variability of the summer climate in the western Tianshan Mountains has been widely identified. In contrast, little is known about the interdecadal variability and related mechanisms of the spring EHEs. Therefore, this research is mainly concerned with the following two questions: What is the interdecadal variability of the EHEs and the associated atmospheric circulation characteristics in the western Tianshan Mountains? What are the mechanisms of the interdecadal variability of the EHEs in the western Tianshan Mountains and the possible influencing factors?.

## 2. Data and Methods

*2.1. Data.* The data used in this study consist of three parts. The daily average temperature at 824 stations provided by the National Climate Center, China Meteorological Administration, is used to analyze the spatial distribution and interdecadal variation of the EHEs, widely used to investigate climate characteristics in China. The monthly (daily) reanalysis data from the National Centers for Environmental Prediction/National Center for Atmospheric Research include the cloud-forcing net solar radiation flux and net surface heat flux, net surface shortwave and long-wave radiation, net surface sensible heat flux and surface latent heat net flux, with a horizontal resolution (Gaussian grid) of $92 \times 192$ ($94 \times 192$). In addition, for variables, i.e., geopotential height, sea level pressure, air temperature, horizontal wind, vertical velocity, relative humidity, and specific humidity, the horizontal resolution of these data is $2.5° \times 2.5°$, and the vertical levels from 1000 hPa to 100 hPa are 11, namely, 1000 hPa, 925 hPa, 850 hPa, 700 hPa, 600 hPa, 500 hPa, 400 hPa, 300 hPa, 250 hPa, 200 hPa, 150 hPa, and 100 hPa. Analysis of the surface heat flux anomalies and atmospheric circulation anomalies related to the EHEs is done using the aforementioned variables from the reanalysis data. The monthly average SST provided by the Hadley Center of the UK Meteorological Office, with a horizontal resolution of $1.0° \times 1.0°$, is used to analyze the possible relationship between the SST anomalies and the EHEs. The spring period in this study is from March to May, and all data span the period 1979–2019.

*2.2. Definition of Extreme High-Temperature Events (EHEs).* In this study, the relative threshold method is adopted to define the EHEs at single stations, i.e., using a percentage threshold method to determine the standard of the EHEs. This method can take into account the different climatic conditions in different regions and has been used in many previous studies [12, 25, 36]. Specifically, the temperature series from 1979 to 2019 at each station are extracted, and the 90th percentile is selected as the threshold. If the temperature values at a station exceed this threshold, they are recorded as the EHEs at this station. The western Tianshan Mountains are defined within the area of 37°N–44°N, 74°E–82°E. A regional EHE is defined based on the regional average of the EHEs at stations in the western Tianshan Mountains.

*2.3. Statistical Methods.* The comprehensive analysis is used in this research to investigate the anomalies of circulations and the SST in different periods, and the Student's $t$-test at the 95%/99% confidence level is performed to estimate the significance of these anomalies. The sliding $t$-test method is

used to examine interdecadal variability. The vertical integration of whole-layer water vapor flux can be calculated by the following equation:

$$Q = \frac{1}{g} \int_{p}^{P_s} q V \mathrm{d}p,\qquad(1)$$

where $g$ denotes the acceleration of gravity, $q$ the specific humidity, $V$ the horizontal wind vector, and $P_s$ the surface pressure. $P_s$ is set to 300 hPa. The atmospheric water vapor content can be expressed by $Q = \int_{p}^{P_s} q\mathrm{d}p$.

## 3. Results and Discussion

### 3.1. Interdecadal Variations of the Frequency of the Spring EHEs.
Figure 1(a) shows the threshold distribution of spring EHEs in the western Tianshan Mountains. The large-value areas are distributed to the east of the western Tianshan Mountains. The number of the spring EHEs shows that the high-frequency values of the EHEs are mainly distributed along the Tarim River in the south of the western Tianshan Mountains (Figure 1(b)). The time series of the regional EHEs in the western Tianshan Mountains displays an abrupt increase after the mid-1990s (Figure 1(c)). Before the mid-1990s, the EHE days were 8.28 day (year)$^{-1}$, while after the mid-1990s, the EHE days increased to 12.06 day (year)$^{-1}$, with an average increasing rate of 1.27 day (decade)$^{-1}$.

Sliding $t$-test results are analyzed to determine the year of an abrupt change, and they show that the frequency of EHE abruptly changed in 1996 (Figure 1(d)). Further analyzing the abrupt change at each station in the western Tianshan mountains (Figure 1(e)) to determine that the year of abrupt change in the region (Figure 1(d)) is not caused by errors at individual stations in individual years. Figure 1(e) demonstrates that the variation trend of EHE frequency at almost all stations had a mutation around 1996. Hence, in order to more thoroughly analyze the interdecadal variation of the EHEs and explore the associated mechanisms, the period of 1979–1995 is considered the inactive period (P1), 2000–2015 as the active period (P2), and 1995–2000 as the transition period.

### 3.2. Circulation Anomalies Related to the Interdecadal Variation of the Spring EHEs

#### 3.2.1. Surface Heat Flux.
Surface thermodynamic efficiency is impacted by the surface heat flux, which has the greatest influence on surface temperature [37]. Figure 2 displays the composite of surface heat flux between P2 and P1 periods. The western Tianshan Mountains have positive net surface heat flow anomalies (Figure 2(a)). This interdecadal variation provides favorable conditions for the increase of spring EHEs. The net surface heat flux (Figure 2(a)) consists of net surface long-wave radiation (Figure 2(b)) and short-wave radiation (Figure 2(c)), and net surface latent (Figure 2(d)) and sensible (Figure 2(e)) heat fluxes. From Figure 2(c), it can be found that the net short-wave radiation shows a positive anomaly in the western Tianshan Mountains, indicating that more solar radiation reaches and heats the surface. In addition, the net surface sensible heat flux in this area also displays a significant positive anomaly (Figure 2(e)), which is beneficial for the accumulation of the positive anomaly of the net surface heat flux (Figure 2(a)). Both the net surface latent heat flux (Figure 2(d)) and the net surface long-wave radiation (Figure 2(b)) exhibit negative anomalies that do not contribute to the net surface heat flux's positive anomaly (Figure 2(a)). The above results indicate that the net surface heat flux in the western Tianshan Mountains is mainly affected by the surface short-wave radiation and sensible heat flux. The reasons for the increase in short-wave radiation and sensible heat flux are discussed further in the following sections.

#### 3.2.2. Water Vapor Conditions and Circulations.
Sufficient water vapor and atmospheric ascending motion facilitate the increase of clouds, which can reduce the solar radiation reaching the surface and affect the surface temperature. Figure 3 presents the composite fields of the 850 hPa vertical velocity, 850 hPa relative humidity, and net solar flux forced by clouds between the P2 and P1 periods. The descending motion (Figure 3(a)) and the decreased water vapor (Figure 3(b)) reduce the cloud cover, resulting in the positive anomaly of cloud-forced net solar radiation (Figure 3(c)). Therefore, the surface short-wave radiation and sensible heat increase (Figures 2(c) and 2(e)), and the surface heat flux increases (Figure 2(a)), which is conducive to the increase in the surface temperature and the occurrence of the EHEs. The causes of atmospheric dryness and ascending motion in the western Tianshan Mountains are analyzed in the following sections.

The net surface latent heat flux in the western Tianshan Mountains shows a negative anomaly (Figure 2(d)), indicating that there is more upward surface latent heat flux, i.e., more water vapor evaporation. Therefore, the dry atmosphere in this area (Figure 3(b)) may not be caused by the local water vapor evaporation but by the water vapor transport. Vertically integrated water vapor flux and water vapor flux divergence between the P2 and P1 periods are shown as composite fields in Figure 4, respectively. The results indicate a westward path of water vapor transport (Figure 4(a)). However, water vapor is not transported to the western Tianshan Mountains, and this region is in a water vapor divergence area, which may lead to a decrease in atmospheric water vapor content in the western Tianshan Mountains (Figure 4(b)).

The anomalous water vapor transport over the western Tianshan Mountains is closely associated with large-scale circulation anomalies. Figure 5(a) depicts the composite field of the 500 hPa geopotential height difference between P2 and P1 periods, which is characterized by an anomalous high pressure over the Iranian Plateau to western China and resembles the distribution pattern of vertically integrated water vapor transport. At 100 hPa (Figure 5(b)), there is also an anomalous anticyclone over the Iranian plateau. The water vapor and atmospheric circulations in the western Tianshan Mountains are affected by this deep anomalous high pressure system (Figure 5(b)).
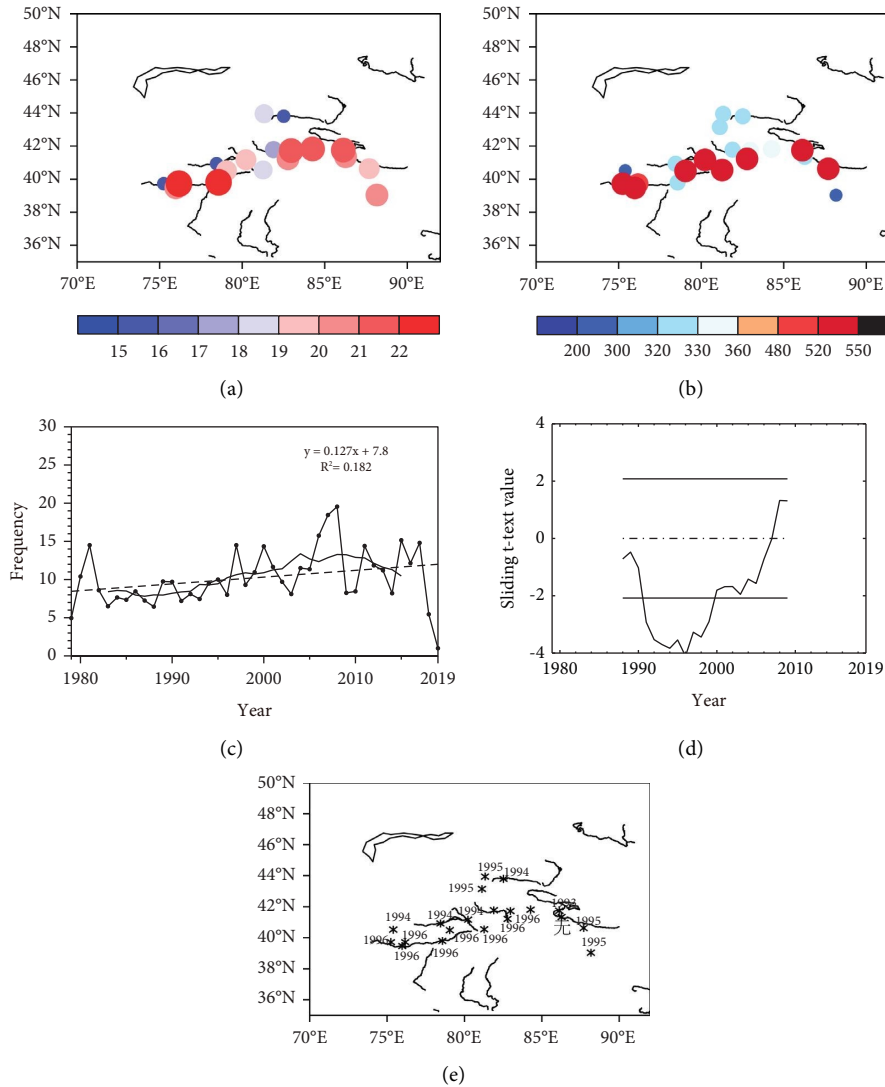
FIGURE 1: The distributions of (a) the spring extreme high-temperature event (EHEs) threshold (˚C) and (b) the extreme EHE frequency (times), (c) the series of the regional average EHE frequency (times) in the western Tianshan mountains in 1979–2019, the 21-year sliding and linear trends, (d) the sliding $t$-test results of the regional EHE frequency, and (e) the sliding $t$-test results of the EHE frequency at each station. The bold curves in Figures 1(a) and 1(b) denote the four-level river distribution.

The anomalous Iranian high is located in the subtropical high belt (Figures 5(a) and 5(b)), with a strong descending motion in the troposphere (Figure 6(a)). The difference in meridional circulation over this region between the P2 and P1 periods shows an anomalous ascending motion near the equator and an anomalous descending motion near the subtropics (Figure 6(b)), which implies a strengthening of the Hadley circulation. The Iranian Plateau is located in the descending branch of the Hadley circulation, which means that the abnormal Iranian high is mainly dynamic. The warming effect of upper-layer air sinking is the main reason for maintaining the high pressure center [38].

3.3. *Relationship between the EHEs and Anomalous SST.* Air-sea interactions significantly impact atmospheric circulation [39, 40]. The discussion continues on whether the tropical and temperate oceans affect the anomalous Iranian

high system. The regression of the SST onto the EHE index was calculated to investigate the potential influence of anomalous SST (Figure 7). These findings indicate that EHEs are highly connected to SST in the Atlantic, Indian, and Pacific oceans. In addition, the key oceanic areas related to the Iranian high are similar, except that the Indian Ocean shows significant positive anomalies. However, the warming of the Indian Ocean is weaker than that of the Pacific Ocean, and there is still a zonal temperature gradient (Figure S1). In particular, the Pacific Ocean is characterized by negative anomalies over the tropical eastern and northern Pacific and positive anomalies over the tropical western Pacific, corresponding to the PDO's negative phase (Figure 7). Additionally, positive anomalies over the eastern and northern Atlantic Oceans correspond to the positive phase of the AMO (Figure 7). Therefore, we determined the correlation between the ECEs and ocean indices to confirm their
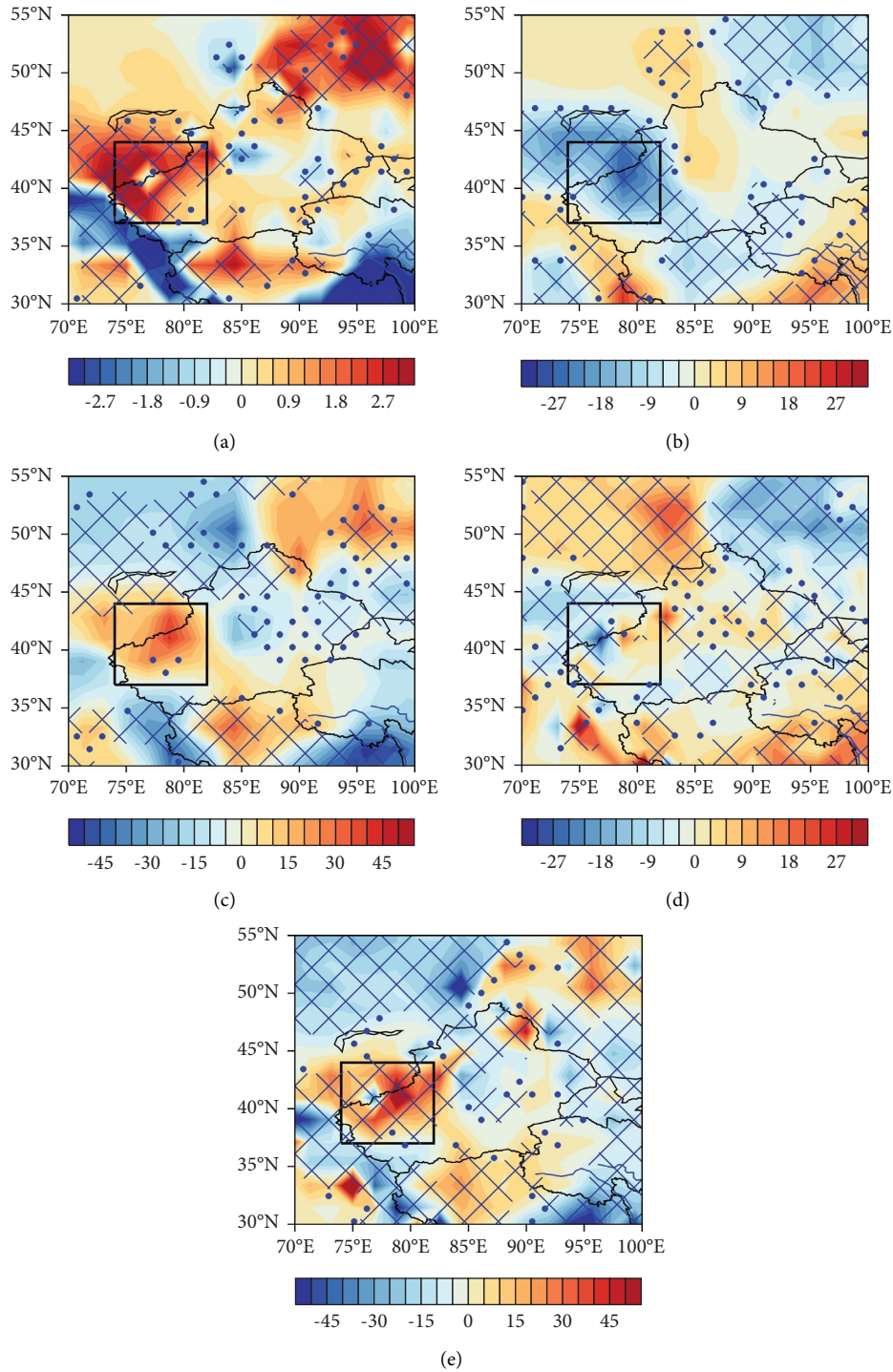
FIGURE 2: Difference in the spring average (a) net surface heat flux (W·m$^{-2}$), (b) net surface long-wave radiation (W·m$^{-2}$), (c) net surface short-wave radiation (W·m$^{-2}$), (d) net surface latent heat flux and (W·m$^{-2}$), and (e) net surface sensible heat flux (W·m$^{-2}$) in the between EHE-prone years P2 (2000–2015) and less EHE years P1 (1983–1995) periods (P2 minus P1). The grids and dots represent the values passing the significance test at the 99% confidence level and the 95% confidence level, respectively, and black boxes denote the region of the western Tianshan Mountains.

relationship (Table 1). The 9-year running mean of the spring mean PDO index and EHE index showed a correlation coefficient of −0.87, significant at the 99% confidence level. Without running, the correlation coefficient is −0.32 at the 95%

confidence level. Similar results were obtained for the AMO index. Overall, the interdecadal variations in the EHEs over the western Tianshan Mountains may have been influenced by SST anomalies in the Indo-Pacific and Atlantic Oceans.
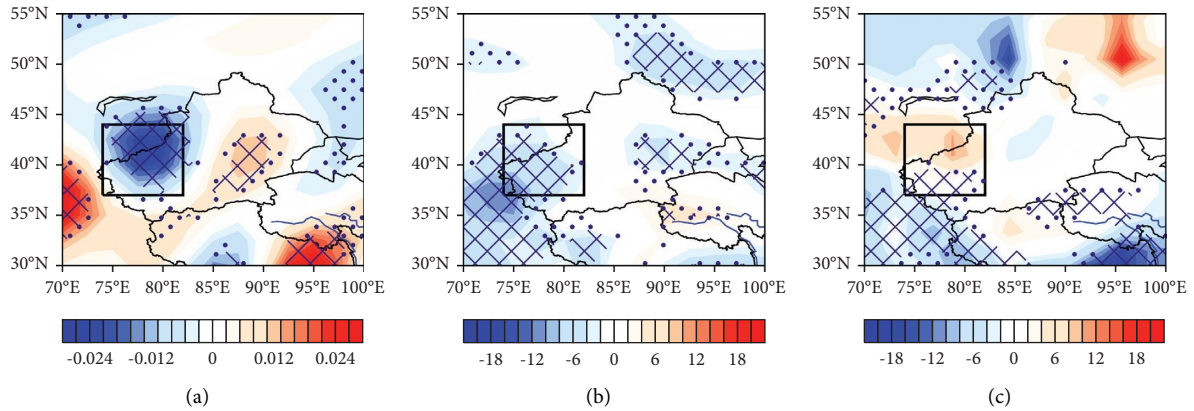
FIGURE 3: Difference in the spring average (a) 850 hPa vertical velocity ($-1 \times \omega$; Pa·s$^{-1}$), (b) 850 hPa relative humidity (%), and (c) cloud-forced net solar radiation (W·m$^{-2}$) between P2 and P1 periods. The grids and dots represent the values passing the significance test at the 99% confidence level and the 95% confidence level, respectively.
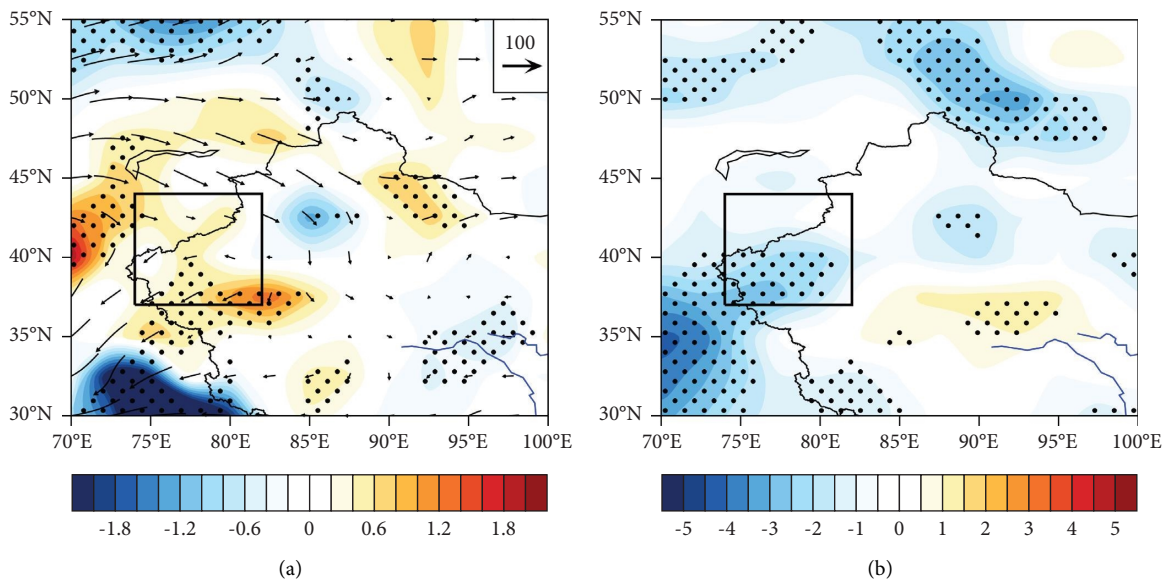


FIGURE 4: Difference in the spring average (a) and water vapor transport (kg·m$^{-1}$·s$^{-1}$) and water vapor transport divergence ($10^{-5}$ kg·m$^{-2}$·s$^{-1}$) (b) whole-layer water vapor content (kg·m$^{-2}$) between P2 and P1 periods. The dots represent the values passing the significance test at the 95% confidence level.
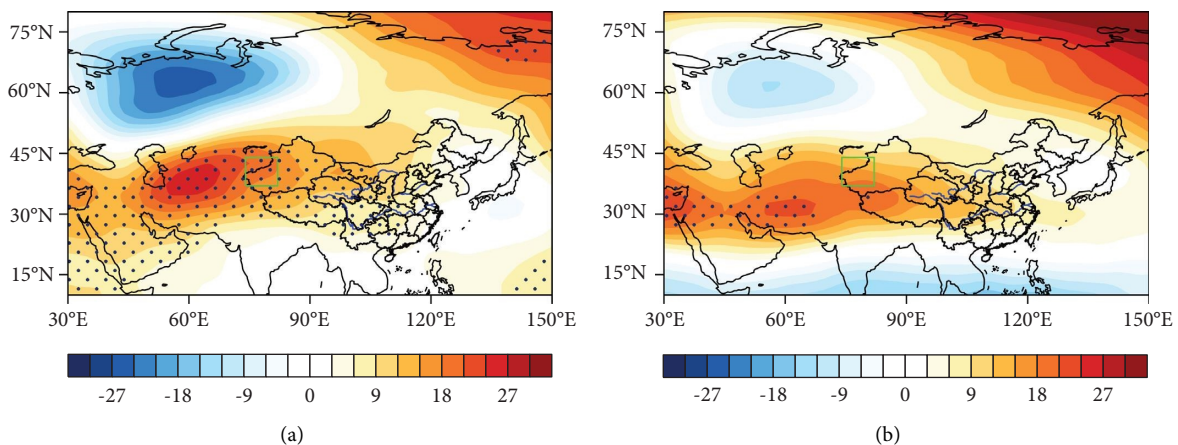


FIGURE 5: Difference in the spring average (a) 500 hPa and (b) 100 hPa geopotential height (train the) between P2 and P1 periods. The dots represent the values passing the significance test at the 95% confidence level.

FIGURE 6: (a) The difference in the spring average zonal circulation (vectors) and vertical velocity (shaded areas; Pa·s$^{-1}$) averaged within 25°N–35°N, and (b) the difference in meridional circulation (vectors) and vertical velocity (shaded areas; Pa·s$^{-1}$) averaged within 60°E–75°E between P2 and P1 periods.
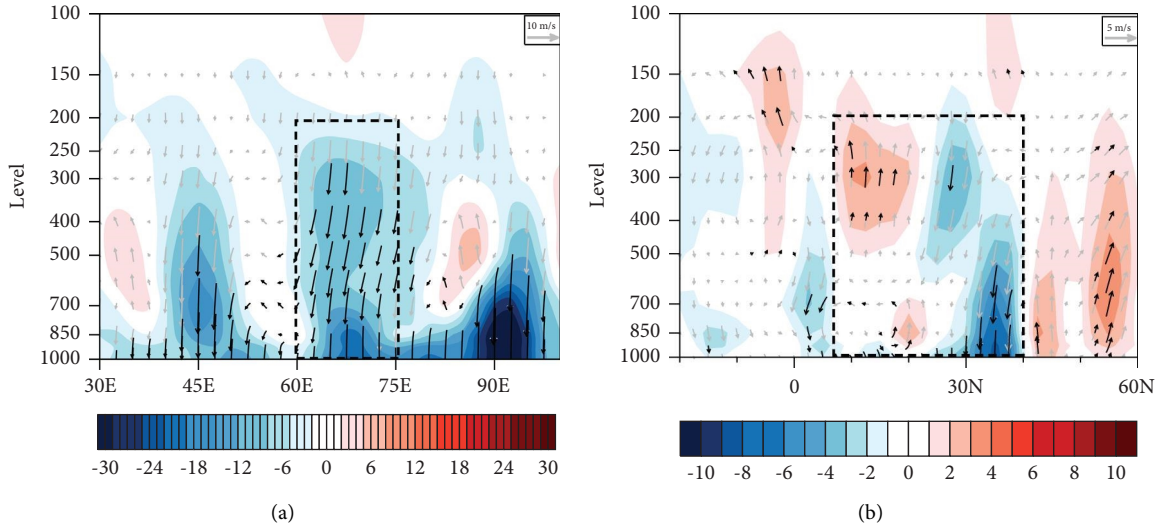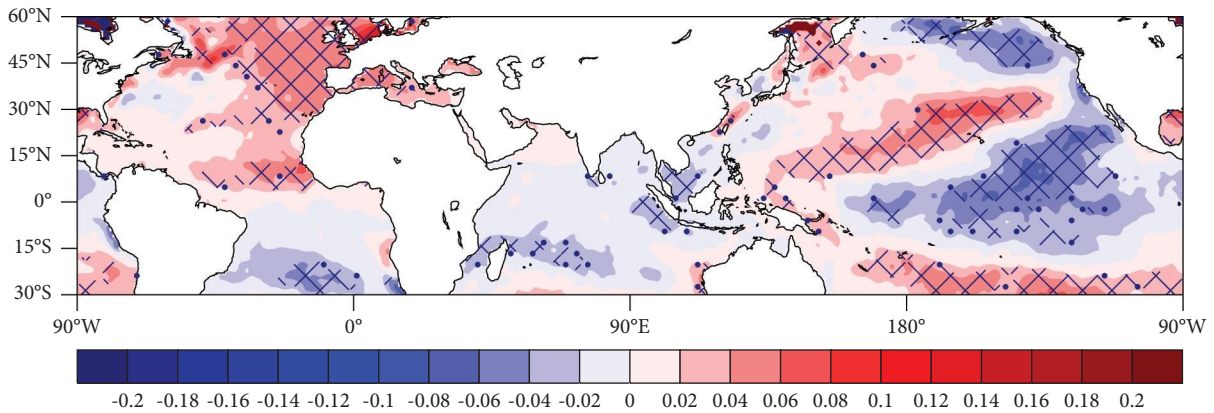


FIGURE 7: Regression of SST in spring with regard to EHEs index from 1979 to 2019 (°C). The dots denote the regression coefficient significant at the 95% confidence level based on the Student's $t$-test.

TABLE 1: The correlation coefficient between the ocean index and EHEs index.

| | AMO | NAO | Nino1 + 2 | Nino3.4 | Nino3 | Nino4 | PDO |
|---|---|---|---|---|---|---|---|
| $r$ | 0.33* | 0.003 | −0.11 | −0.31 | −0.24 | −0.21 | −0.32* |
| $r_{run}$ | 0.93* | −0.78* | −0.49* | −0.58* | −0.52* | −0.18 | −0.87* |

The asterisks denote the correlation coefficient significant at the 95% confidence level based on Student's $t$-test.

*3.3.1. The Influence of Indo-Pacific Anomalous SST.* The differences in SST between P2 and P1 were calculated to investigate the interdecadal variation in the Indo-Pacific SST. Consistent with the frequent occurrence of EHEs, there was anomalous warming over the western Pacific to the northern Pacific and anomalous cooling over the tropical

eastern Pacific, both of which corresponded with the negative phase of the PDO (Figure 8(c)), except in the Indo-Pacific sector. The annual mean SST composite (Figure 8(b)) and the PDO annual mean SST composite (Figure 8(d)) over the Pacific were similar to those of the spring SST (Figures 8(a) and 8(c)).

Accompanied by anomalous warming of SST over the western Pacific (Figure 9(a)), there was a significant increase in upward long-wave radiation (Figure 9(b)); thus, wind fields converged at 700 hPa in the lower troposphere (Figure 9(c)) and diverged at 200 hPa in the upper troposphere (Figure 9(d)). In contrast, the anomalous warming in the western Indian Ocean was weaker than that in the western Pacific (Figure 9(a)), resulting in weaker upward long-wave radiation (Figure 9(b)). Therefore, the wind

FIGURE 8: Difference in (a) spring average SST and (b) annual average SST (unit: °C) between P2 and P1, and (c) and (d) same as (a) and (b) except for between the positive years and negative years of the Pacific decadal oscillation (PDO) index. (a) SST_MAM. (b) SST_annual. (c) PDO_SST_MAM. (d) PDO_SST_annual.
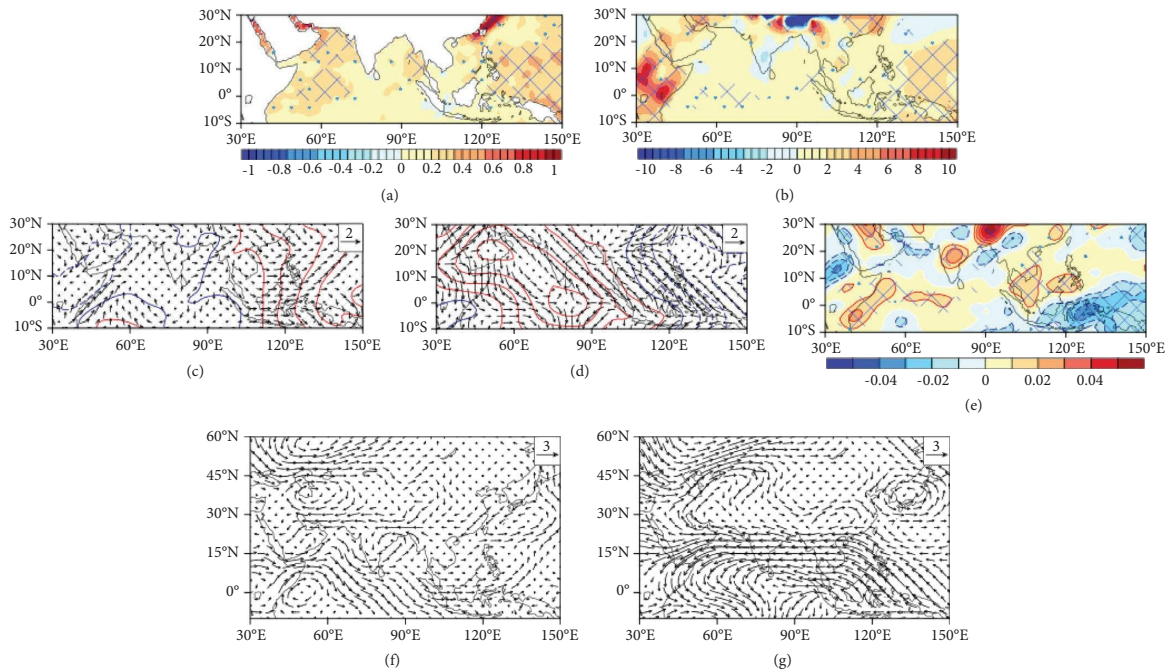


FIGURE 9: Difference in the spring average (a) SST (°C), (b) upward long-wave radiation (W·m$^{-2}$), (c) 700 hPa divergent wind (vectors; m·s$^{-1}$) and velocity potential (line, m·s$^{-2}$), (d) 200 hPa divergent wind and velocity potential, (e) 500 hPa vertical velocity (Pa·s$^{-1}$), (f) 700 hPa horizontal wind (vectors; m·s$^{-1}$), and (g) 200 hPa horizontal wind between P2 and P1 periods. The red line represents a positive value, the blue line represents a negative value in (c), (d), and (e), and the grids and dots represent the values passing the significance test at the 99% confidence level and the 95% confidence level in (a), (b), and (e).
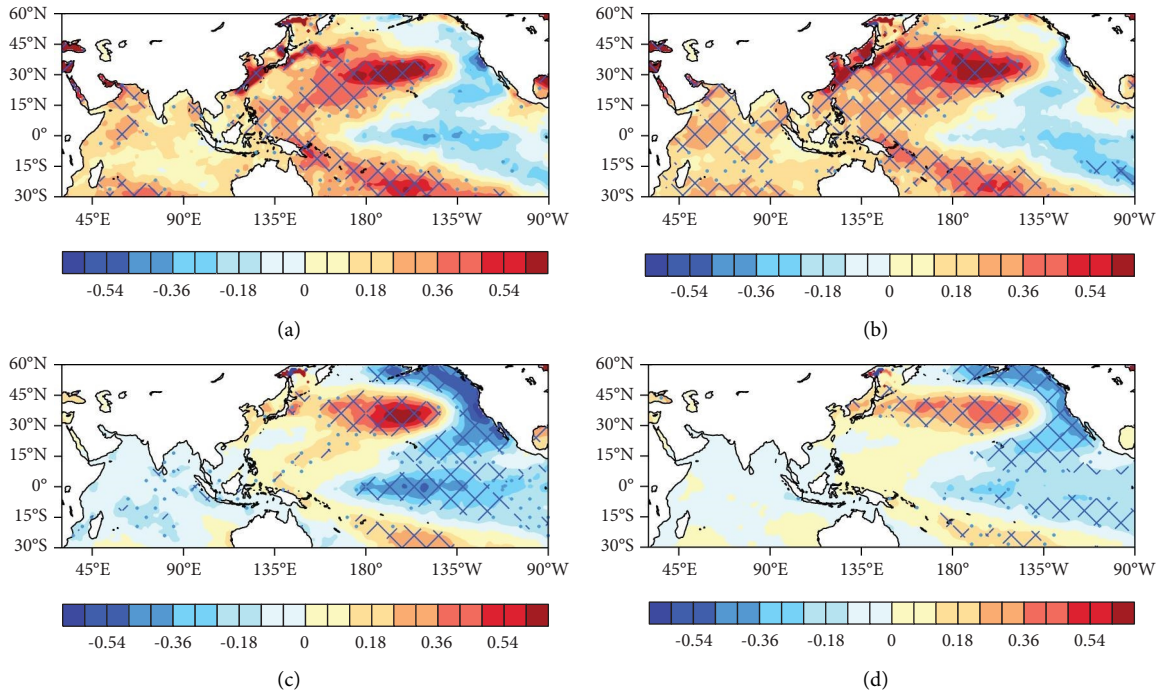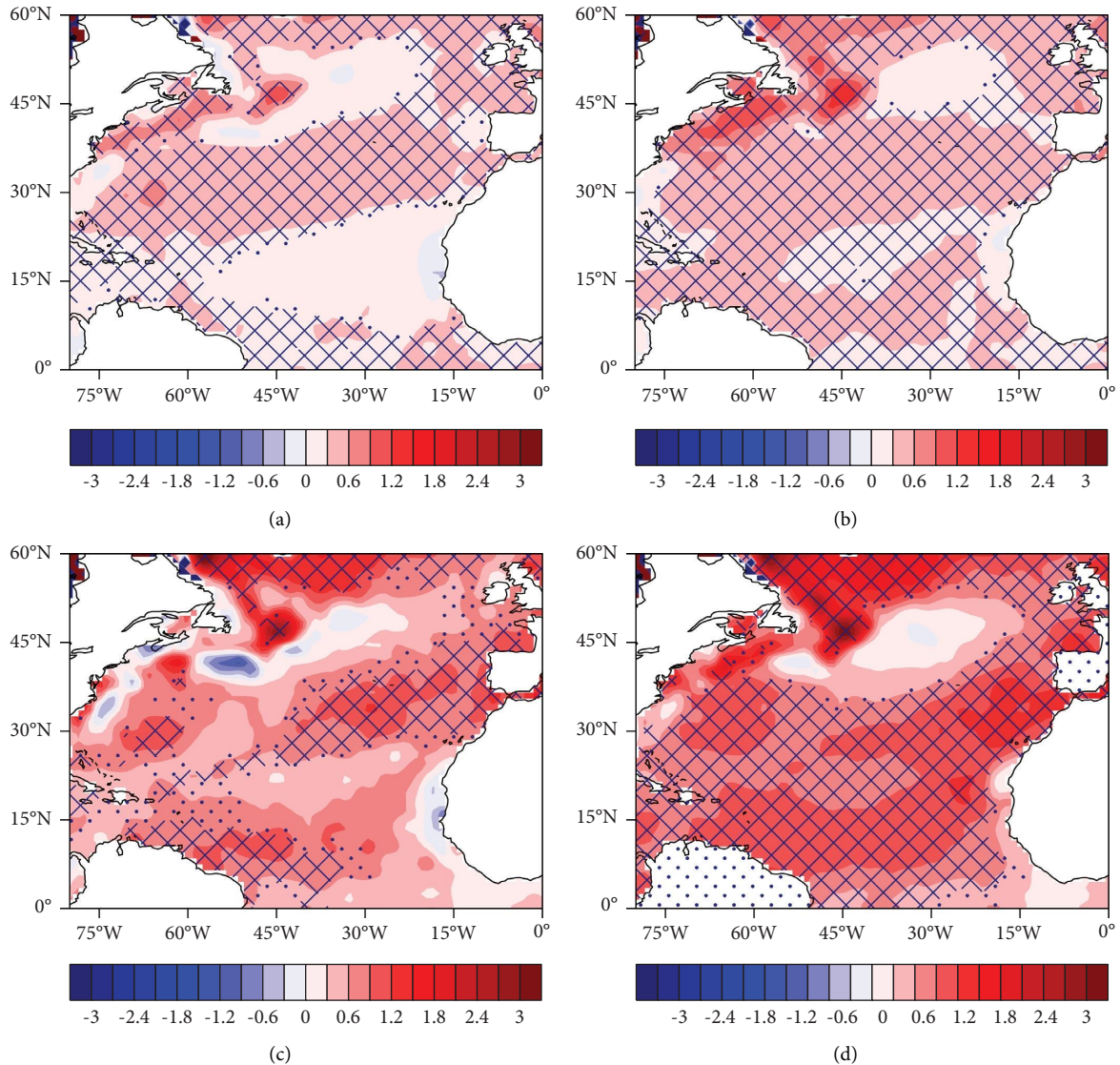
FIGURE 10: Difference in the (a) spring average SST (b) annual average SST (unit: °C) between P2 and P1, and (c) (d) same as (a) (b) except for between the positive years and negative years of the Atlantic multidecadal oscillation (AMO) index. (a) SST_MAM. (b) SST_annual. (c) AMO_SST_MAM. (d) AMO_SST_annual.

converged at 200 hPa in the upper troposphere (Figure 9(d)) and diverged at 700 hPa in the lower troposphere (Figure 9(c)). Based on mass compensation, it can be considered that the troposphere over the tropical western Pacific is controlled by anomalous ascending motion and the troposphere over the tropical western Indian Ocean is influenced by anomalous descending motion (Figure 9(e)), suggesting a strengthened Walker circulation.

Moreover, the lower branch of the Walker circulation at 700 hPa was characterized by westerly anomalies from the western Indian Ocean to the western Pacific (Figure 9(f)), and the upper branch (200 hPa) was characterized by strong easterly anomalies (Figure 9(g)). The upper branch of the Walker circulation strengthened the easterly wind south of the anomalous Iranian high, resulting in pressure

strengthening. In summary, the zonal thermal gradient between the tropical western Pacific and the western Indian Ocean directly affected the zonal vertical circulation and strengthened the anomalous Iranian high [41].

### 3.3.2. The Influence of Atlantic Anomalous SST.

We further focused on the accompanying variations in Atlantic SST to study other factors causing interdecadal variations in anomalous Iranian highs. Figure 10 shows the composite SST in the Atlantic between P2 and P1. Consistent with the frequent occurrence of EHEs, there was anomalous warming over the North Atlantic (Figure 10(a)), corresponding to the positive phase of the AMO (Figure 10(c)). The annual mean SST composite (Figure 10(b)) and AMO's annual mean SST
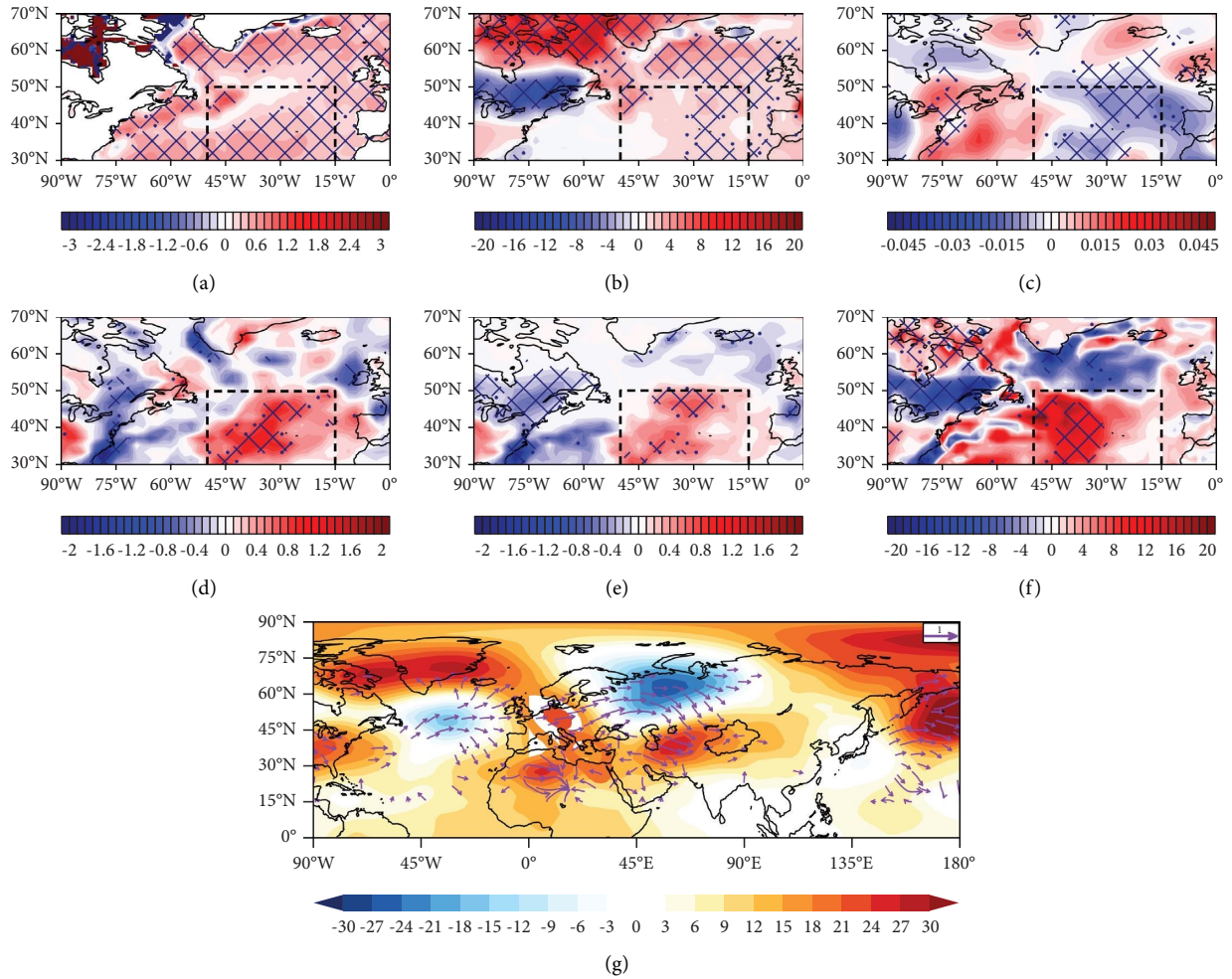
FIGURE 11: Difference in the spring average (a) SST (°C), (b) upward long-wave radiation (W·m$^{-2}$), (c) 500 hPa vertical velocity ($-1 \times \omega$; Pa·s$^{-1}$), (d) precipitation rate (kg·m$^{-2}$·s$^{-1}$), (e) convective precipitation rate at surface (kg·m$^{-2}$·s$^{-1}$), (f) upward surface latent heat net flux (W·m$^{-2}$), and (g) 500 hPa geopotential height (shading; gpm) and the corresponding wave activity flux (vectors; unit: m$^2$·s$^{-2}$) between P2 and P1. The grids and dots represent the values passing the significance test at the 99% confidence level and the 95% confidence level based on the Student's $t$-test, respectively.

composite (Figure 10(d)) over the Pacific were similar to those of the spring SST (Figures 10(a) and 10(c)).

Accompanied by the anomalous warming of SST over the Atlantic (Figure 11(a)), there was a significant increase in upward long-wave radiation (Figure 11(b)), inducing anomalous ascension in the overlying atmosphere (Figure 11(c)). Owing to the anomalous ascent, precipitation increased (Figure 11(d)), mainly convective precipitation (Figure 11(e)). Therefore, the latent heat increased (Figure 11(f)) and heated the atmosphere, favoring the persistence of a negative potential height anomaly over the North Atlantic (Figure 11(g)). The interaction between air and sea over the North Atlantic triggered a mid-latitude wave train (Figure 11), strengthening the anomalous Iranian high.

In addition, the oceanic front may also affect the negative geopotential height anomaly over the Atlantic Ocean. The change in the oceanic front caused by SST anomalies affects the atmospheric transient eddy [40]. The anomalous warming pattern over the Atlantic (Figure S2(a)) resulted in positive anomalies in meridional SST gradients and sensible heat fluxes over the northern Atlantic (Figures S2(b) and S2(c)), thus enhancing the temperate oceanic front. The low-level atmospheric meridional temperature gradient and, thus, the low-level atmospheric baroclinicity tended to be reinforced when the atmospheric boundary layer adjusted to the strengthened oceanic front (Figures S2(d) and S2(e)), favoring the persistence of a potential negative height anomaly over the Atlantic (figure 11(g)).

FIGURE 12: A schematic diagram illustrating the mechanism through which key oceanic areas influence the EHEs in the western Tianshan mountains by a mid-latitude wave train and walker circulation.

## 4. Conclusions

In this study, the spatial distribution characteristics and interdecadal variation of the EHEs in the western Tianshan Mountain from 1979 to 2019 are analyzed. The possible causes affecting the interdecadal variation of the EHEs are investigated, and the possible relationship between the tropical SST anomaly and the EHEs is discussed. The main conclusions are as follows:

(1) The spring EHEs in the western Tianshan Mountains showed interdecadal variability in the mid-1990s, characterized by less in 1983–1996 and more in 2000–2015. In addition, the spatial distribution of the EHEs has local characteristics, with a high occurrence frequency in the area along the Tarim River.

(2) Compared with the atmospheric circulations during 1983–1996, there was a deep dynamic high pressure system over the Iranian Plateau during 2000–2015. Under the control of the anomalous high pressure system, the atmospheric water vapor content is lower over the western Tianshan area, and this region is controlled by atmospheric descending motion. On the one hand, with the descending motion, the adiabatic heating heats the atmosphere in the lower layers. On the other hand, dry atmospheric conditions with descending motion are not conducive to the increase of cloud cover, and thus, the net solar radiation forced by clouds increases correspondingly. In addition, the short-wave radiation flux and sensible heat flux reaching the surface increase, and the net surface heat flux increases cumulatively. These conditions are conducive to the increase of the surface temperature and the occurrence of EHEs.

(3) The comprehensive analysis of the SST suggests that the zonal SST difference between the tropical western Pacific and the western Indian Ocean directly strengthens Walker circulation. The western tropical Pacific Ocean is controlled by atmospheric ascending motion, and the western tropical Indian Ocean is controlled by descending motion. The circulations in the lower troposphere are dominated by westerly anomalies, and those in the upper troposphere are dominated by easterly anomalies. The upper troposphere's easterly anomalies strengthen the easterly airflow south of the anomalous Iranian high, thereby strengthening the high pressure.

(4) The anomalous Iranian high is also associated with the atmospheric wave trains at midlatitude, which are related to different air–sea interaction in the Atlantic. The anomalous warming of Atlantic SST inducing convective precipitation was increased and the oceanic front was enhanced. The anomalous convective precipitation induces more latent heat release, which are led to negative potential height anomaly over Atlantic and trigger a midlatitude wave train. In addition, the enhanced oceanic front induces the atmospheric baroclinicity stronger and synoptic transient eddy activities frequently, which favors the persistence of a negative potential height anomaly over the North Atlantic (Figure 12).

In this study, we discuss the possible effects of SST anomalies in the tropical Pacific and Indian Oceans on the local high pressure over the Iranian Plateau. Previous studies have also mentioned that Indo-West Pacific warming was one of the factors affecting the interdecadal variations of atmospheric circulations in the late 1970s [42]. Additionally, the changes in circulations and water vapor distribution caused by the phase transition of the Pacific Decadal Oscillation further affect the EHEs in Asia. The Atlantic SST anomalies excite the mid-latitude wave train through air-sea

interactions, thereby influencing the Eurasian atmospheric circulations and extreme temperature and precipitation events [43]. In addition, recent studies have increasingly suggested Pacific-Atlantic interaction since the early 1990s [44]. The spring Atlantic Ocean actively influences the winter Pacific climate and ENSO variability by influencing subtropical teleconnections on the intertropical convergence zone (ITCZ), similar to a discharging capacitor [45]. The possibility of a global warming trend interfering with the prior positive phase of the AMO (during the 1930s–1960s) could explain why the previous positive phase of the AMO (during the 1930s–1960s) was not accompanied by heightened Atlantic-Pacific interactions [45]. Further investigating the relationship between these factors and EHEs can contribute to a comprehensive understanding of the formation mechanisms of the EHEs over the western Tianshan Mountains.

In terms of the diagnostic analysis in this study, the seasonal mean data are used to determine the relationship between oceanic and atmospheric anomalies. This relationship can be understood as an equilibrium state due to the interactions among these fields. Comparative analyses of multi-source data and model simulation would make the results more robust, which will be carried out in the future.

## Data Availability

The NCEP/NCAR reanalysis data is accessible at https://psl. noaa.gov/data/gridded/data.ncep.reanalysis.html. The monthly SST data derived from the Met Office Hadley Center can be downloaded online at https://www.metoffice. gov.uk/hadobs/hadisst/. Other data used to support the findings of this study are available from the corresponding author upon request.

## Conflicts of Interest

The authors declare that there are no conflicts of interest regarding the publication of this article.

## Acknowledgments

## Supplementary Materials

Supplementary Figure 1: regression of SST in spring with regard to the Iranian high index from 1979 to 2019 ($^\circ$C). The dots denote the regression coefficient significant at the 95% confidence level based on the Student's $t$ test. Supplementary Figure 2: difference in the spring average (a) SST ($^\circ$C), (b) meridional SST gradient ($10^{-6}$ k·m$^1$), (c) net surface sensible heat flux (W·m$^{-2}$), (d) surface 2-m air temperature ($^\circ$C), and (e) meridional gradient of surface 2-m air temperature ($10^{-6}$ k·m$^{-1}$) between P2 and P1. (*Supplementary Materials*)

## References

[1] IPCC, "Summary for policymakers. in: global warming of 1.5$^\circ$C. An IPCC Special Report on the Impacts of Global Warming of 1.5$^\circ$C above Pre-industrial Levels and Related Global Greenhouse Gas Emission Pathways," in *The Context of Strengthening the Global Response to the Threat of Climate Change, Sustainable Development, and Efforts to Eradicate Poverty*, V. Masson-Delmotte, P. Zhai, H. O. Pörtner et al., Eds., IPCC, Geneva, Switzerland, 2018.

[2] Y. Sun, X. Zhang, F. W. Zwiers et al., "Rapid increase in the risk of extreme summer heat in Eastern China," *Nature Climate Change*, vol. 4, no. 12, pp. 1082–1085, 2014.

[3] M. A. Borg, J. Xiang, O. Anikeeva, and P. Bi, "Occupational heat stress and economic burden: a review of global evidence," *ISEE Conference Abstracts*, vol. 2021, no. 1, Article ID 110781, 2021.

[4] R. García-Herrera, J. Díaz, R. M. Trigo, J. Luterbacher, and E. M. Fischer, "A review of the European summer heat wave of 2003," *Critical Reviews in Environmental Science and Technology*, vol. 40, no. 4, pp. 267–306, 2010.

[5] D. Barriopedro, E. M. Fischer, J. Luterbacher, R. M. Trigo, and R. García-Herrera, "The hot summer of 2010: redrawing the temperature record map of europe," *Science*, vol. 332, no. 6026, pp. 220–224, 2011.

[6] C. Wang, J. Zheng, W. Lin, and Y. Wang, "Unprecedented heatwave in western North America during late june of 2021: roles of atmospheric circulation and global warming," *Advances in Atmospheric Sciences*, vol. 40, no. 1, pp. 14–28, 2023.

[7] S. Gao, J. Guo, S. Zhao, Y. Zhang, and Y. Pan, "The impacts of "higher-temperature" on wheat growth and yield in China," *Chinese Journal of Atmospheric Sciences*, vol. 20, no. 5, pp. 599–605, 1996.

[8] W. Mao, J. Yao, J. Chen, S. J. Li, H. J. Li, and Y. Z. Shi, "Change characteristics of extreme temperature-rising process in the east pamirs during 1961—2017," *Arid Zone Research*, vol. 36, no. 6, pp. 1368–1378, 2019.

[9] A. F. Hamlet and D. P. Lettenmaier, "Effects of 20th century warming and climate variability on flood risk in the western U.S," *Water Resources Research*, vol. 43, no. 6, 2007.

[10] Y. Z. Pan, J. A. Wang, and D. Y. Gong, "Changes in extreme daily mean temperatures in summer in eastern China during 1955–2000," *Theoretical and Applied Climatology*, vol. 77, no. 1-2, pp. 25–37, 2004.

[11] H. Wang and S. He, "The North China/Northeastern Asia severe summer drought in 2014," *Journal of Climate*, vol. 28, no. 17, pp. 6667–6681, 2015.

[12] B. Zhu, B. Sun, H. Li, and H. Wang, "Interdecadal variations in extreme high–temperature events over southern China in the early 2000s and the influence of the Pacific decadal oscillation," *Atmosphere*, vol. 11, no. 8, p. 829, 2020.

[13] J. Q. Sun, H. J. Wang, and W. Yuan, "Decadal variability of the extreme hot event in China and its association with atmospheric circulations," *Climatic and Environmental Research (in Chinese)*, vol. 16, no. 2, pp. 199–208, 2011.

[14] Y. Shi, Y. Shen, and R. Hu, "Preliminary study on signal, impact and foreground of climatic shift from warm-dry to warm-humid in Northwest China," *Journal of Glaciology and Geocryology*, vol. 24, no. 3, pp. 219–226, 2002.

[15] G. Blöschl, J. Hall, J. Parajka et al., "Changing climate shifts timing of European floods," *Science*, vol. 357, no. 6351, pp. 588–590, 2017.

[16] L. Ren, T. Zhou, and W. Zhang, "Attribution of the record-breaking heat event over Northeast Asia in summer 2018: the role of circulation," *Environmental Research Letters*, vol. 15, no. 5, Article ID 054018, 2020.

[17] R. Chen and R. Lu, "Comparisons of the circulation anomalies associated with extreme heat in different regions of eastern China," *Journal of Climate*, vol. 28, no. 14, pp. 5830–5844, 2015.

[18] R. Chen, Z. Wen, and R. Lu, "Interdecadal change on the relationship between the mid-summer temperature in South China and atmospheric circulation and sea surface temperature," *Climate Dynamics*, vol. 51, no. 5-6, pp. 2113–2126, 2018.

[19] M. Li, D. Luo, Y. Yao, and L. Zhong, "Large-scale atmospheric circulation control of summer extreme hot events over China," *International Journal of Climatology*, vol. 40, no. 3, pp. 1456–1476, 2020.

[20] Q. Tong, Y. Huang, M. Duan, and Q. Zhao, "Possible contribution of the PDO to the eastward retreat of the western pacific subtropical high," *Atmospheric and Oceanic Science Letters*, vol. 14, no. 1, Article ID 100005, 2021.

[21] R. Chen, Z. Wen, and R. Lu, "Evolution of the circulation anomalies and the quasi-biweekly oscillations associated with extreme heat events in southern China," *Journal of Climate*, vol. 29, no. 19, pp. 6909–6921, 2016.

[22] M. Luo and N. C. Lau, "Amplifying effect of ENSO on heat waves in China," *Climate Dynamics*, vol. 52, no. 5-6, pp. 3277–3289, 2019.

[23] K. Hu, G. Huang, and R. Wu, "A strengthened influence of ENSO on august high temperature extremes over the southern yangtze river valley since the late 1980s," *Journal of Climate*, vol. 26, no. 7, pp. 2205–2221, 2013.

[24] C. Qian, W. Zhou, X. Q. Yang, and J. C. L. Chan, "Statistical prediction of non-Gaussian climate extremes in urban areas based on the first-order difference method," *International Journal of Climatology*, vol. 38, no. 6, pp. 2889–2898, 2018.

[25] B. Zhu, B. Sun, and H. Wang, "Increased interannual variability in the dipole mode of extreme high-temperature events over east China during summer after the early 1990s and associated mechanisms," *Journal of Climate*, vol. 35, no. 4, pp. 1347–1364, 2022.

[26] K. Hu, G. Huang, and R. Huang, "The impact of tropical Indian ocean variability on summer surface air temperature in China," *Journal of Climate*, vol. 24, no. 20, pp. 5365–5377, 2011.

[27] K. Deng, X. Jiang, C. Hu, and D. Chen, "More frequent summer heat waves in southwestern China linked to the recent declining of Arctic sea ice," *Environmental Research Letters*, vol. 15, no. 7, Article ID 074011, 2020.

[28] H. Li, H. Chen, H. Wang, J. Sun, and J. Ma, "Can barents sea ice decline in spring enhance summer hot drought events over northeastern China?" *Journal of Climate*, vol. 31, no. 12, pp. 4705–4725, 2018.

[29] X. Han, L. Zhao, J. Yao, and Q. Yang, "Temporal and spatial distribution of the extreme high temperatures in arid regions of Northwest China," *Desert and Oasis Meteorology*, vol. 13, no. 4, pp. 17–23, 2019.

[30] H. Li, "Characteristics of maximum temperature and high temperature days in summer in aletai in past 47 years," *Desert and Oasis Meteorology*, vol. 8, no. 3, pp. 56–60, 2014.

[31] M. Wang, J. Zhou, and Y. Xie, "Climate characteristics and variation trend of the megathermal days in kelamayi," *Desert and Oasis Meteorology*, vol. 4, no. 5, pp. 27–30, 2010.

[32] W. Mao, P. Chen, and Y. Shen, "Characteristics and effects of the extreme maximum air temperature in the summer of 2015 in Xinjiang under global warming," *Journal of Glaciology and Geocryology*, vol. 38, no. 2, pp. 291–304, 2016.

[33] F. Qi and X. Pan, "Comparative analysis of circulation characteristics and variations of high temperature between fuhai and fuyun," *Desert and Oasis Meteorology*, vol. 5, no. 5, pp. 52–54, 2011.

[34] B. Zhu, X. Yang, P. Rioual et al., "Hydrogeochemistry of three watersheds (the erlqis, zhungarer and Yili) in northern Xinjiang, NW China," *Applied Geochemistry*, vol. 26, no. 8, pp. 1535–1548, 2011.

[35] G. Wang, D. Yang, and C. Xiong, "Dynamic evaluation and spatial distribution characteristics of agricultural green development level in restricted development areas: a case study of Yili River valley, China," *Polish Journal of Environmental Studies*, vol. 30, no. 5, pp. 4255–4266, 2021.

[36] S. Chen, R. Wu, and Y. Liu, "Dominant modes of interannual variability in eurasian surface air temperature during boreal spring," *Journal of Climate*, vol. 29, no. 3, pp. 1109–1125, 2016.

[37] B. Sun, "Seasonal evolution of the dominant modes of the Eurasian snowpack and atmospheric circulation from autumn to the subsequent spring and the associated surface heat budget," *Atmospheric and Oceanic Science Letters*, vol. 10, no. 3, pp. 191–197, 2017.

[38] Q. Yongfu, Z. Qiong, Y. Yonghong, and Z. Xuehong, "Seasonal variation and heat preference of the South Asia high," *Advances in Atmospheric Sciences*, vol. 19, no. 5, pp. 821–836, 2002.

[39] G. Huang, X. Qu, and K. Hu, "The impact of the tropical Indian Ocean on South Asian High in boreal summer," *Advances in Atmospheric Sciences*, vol. 28, no. 2, pp. 421–432, 2011.

[40] J. Fang and X. Q. Yang, "Structure and dynamics of decadal anomalies in the wintertime midlatitude North Pacific ocean–atmosphere system," *Climate Dynamics*, vol. 47, no. 5-6, pp. 1989–2007, 2016.

[41] H. Annamalai, P. Liu, and S. P. Xie, "Southwest Indian Ocean SST variability: its local effect and remote influence on asian monsoons," *Journal of Climate*, vol. 18, no. 20, pp. 4150–4167, 2005.

[42] X. Qu and G. Huang, "An enhanced influence of tropical Indian ocean on the South Asia high after the late 1970s," *Journal of Climate*, vol. 25, no. 20, pp. 6930–6941, 2012.

[43] H. Li, S. He, Y. Gao, H. Chen, and H. Wang, "North atlantic modulation of interdecadal variations in hot drought events over Northeastern China," *Journal of Climate*, vol. 33, no. 10, pp. 4315–4332, 2020.

[44] C. Qian, J. Y. Yu, and G. Chen, "Decadal summer drought frequency in China: the increasing influence of the Atlantic Multi-decadal Oscillation," *Environmental Research Letters*, vol. 9, no. 12, Article ID 124004, 2014.

[45] L. Wang, J. Y. Yu, and H. Paek, "Enhanced biennial variability in the Pacific due to Atlantic capacitor effect," *Nature Communications*, vol. 8, no. 1, Article ID 14887, 2017.